The Astrophysical Journal Letters, 976:L28 (14pp), 2024 December 1 https://doi.org/10.3847/2041-8213/ad8b9d

The Truncated Circumgalactic Medium of the Large Magellanic Cloud*

Sapna Mishra[1], Andrew J. Fox[2,3], Dhanesh Krishnarao[4], Scott Lucchini[5,6], Elena D'Onghia[6,7,8], Frances H. Cashman[1,9], Kathleen A. Barger[10], Nicolas Lehner[11], and Jason Tumlinson[1,3]
[1] Space Telescope Science Institute, 3700 San Martin Drive, Baltimore, MD 21218, USA; smishra@stsci.edu
[2] AURA for ESA, Space Telescope Science Institute, 3700 San Martin Drive, Baltimore, MD 21218, USA
[3] Department of Physics & Astronomy, Johns Hopkins University, 3400 N. Charles Street, Baltimore, MD 21218, USA
[4] Department of Physics, Colorado College, Colorado Springs, CO 80903, USA
[5] Center for Astrophysics | Harvard & Smithsonian, 60 Garden Street, Cambridge, MA 02138, USA
[6] Department of Physics, University of Wisconsin—Madison, Madison, WI 53706, USA
[7] Department of Astronomy, University of Wisconsin—Madison, Madison, WI 53706, USA
[8] INAF—Osservatorio Astrofisico di Torino, via Osservatorio 20, 10025 Pino Torinese (TO), Italy
[9] Department of Physics, Presbyterian College, Clinton, SC 29325, USA
[10] Department of Physics & Astronomy, Texas Christian University, Fort Worth, TX 76129, USA
[11] Department of Physics and Astronomy, University of Notre Dame, Notre Dame, IN 46556, USA
Received 2024 July 26; revised 2024 October 15; accepted 2024 October 15; published 2024 November 27

Abstract

The Large Magellanic Cloud (LMC) is the nearest massive galaxy to the Milky Way (MW). Its circumgalactic medium (CGM) is complex and multiphase, containing both stripped H I structures like the Magellanic Stream and Bridge and a diffuse warm corona seen in high-ion absorption. We analyze 28 active galactic nucleus sight lines passing within 35 kpc of the LMC with archival Hubble Space Telescope/Cosmic Origins Spectrograph spectra to characterize the cool ($T \approx 10^4$ K) gas in the LMC CGM, via new measurements of UV absorption in six low ions (O I, Fe II, Si II, Al II, S II, and Ni II) and one intermediate ion (Si III). We show that a declining column-density profile is present in all seven ions, with the low-ion profiles having a steeper slope than the high-ion profiles in C IV and Si IV reported by D. Krishnarao et al. Crucially, absorption at the LMC systemic velocity is only detected (in all ions) out to 17 kpc. Beyond this distance, the gas has a lower velocity and is associated with the Magellanic Stream. These results demonstrate that the LMC's CGM is composed of two distinct components: a compact inner halo extending to 17 kpc and a more extended stripped region associated with the Stream. The compactness and truncation of the LMC's inner CGM agree with recent simulations of ram-pressure stripping of the LMC by the MW's extended corona.

Unified Astronomy Thesaurus concepts: Large Magellanic Cloud (903); Galactic and extragalactic astronomy (563); Galaxy dynamics (591); Galaxy physics (612); Magellanic Clouds (990); Magellanic Stream (991); the Milky Way (1054)

Materials only available in the online version of record: machine-readable table

1. Introduction

The Large Magellanic Cloud (LMC), merely 50 kpc away (G. Pietrzyński et al. 2013), is the closest massive galaxy to the Milky Way (MW). Dynamic interactions with the MW and the Small Magellanic Cloud (SMC) are profoundly impacting the LMC and its gaseous circumgalactic medium (CGM). The gaseous structures in this system exhibit complex morphology and structure, as evidenced by the Magellanic Bridge, Magellanic Stream (hereafter the Stream), and Leading Arm, which together with the LMC and SMC are known as the Magellanic System (E. D'Onghia & A. J. Fox 2016 and references therein). The Stream, an approximately 200° long tail of multiphase gas, has been extensively mapped in both neutral hydrogen (M. E. Putman et al. 2003b; C. Brüns et al. 2005; D. L. Nidever et al. 2008, 2010; T. Westmeier 2018) and in ionized gas using ultraviolet (UV) surveys (A. J. Fox et al. 2013, 2014; P. Richter et al. 2013) and Hα surveys (M. E. Putman et al. 2003a; K. A. Barger et al. 2017; J. Bland-Hawthorn et al. 2019; see also D. A. Kim et al. 2024). The Stream is thought to have been stripped out of the Magellanic Clouds, either by tidal forces (M. Fujimoto & Y. Sofue 1977; G. Besla et al. 2012; S. A. Pardy et al. 2018) or ram pressure (B. Moore & M. Davis 1994; J. Diaz & K. Bekki 2011; M. Salem et al. 2015; J. Wang et al. 2019).

In addition to the stripped gas, recent simulations and observations have revealed that the LMC is surrounded by its own diffuse ionized CGM, or "corona." Such a corona is motivated by the high mass of the LMC ($>10^{11}\,M_{\odot}$; D. Erkal et al. 2019; M. S. Petersen & J. Penarrubia 2021; L. L. Watkins et al. 2024) and the need to explain the high mass of ionized gas of the Stream, which was previously not reproduced in tidal or ram-pressure models (S. Lucchini et al. 2020, 2024). Observational evidence for the corona was provided by D. Krishnarao et al. (2022, hereafter K22; see also K. S. de Boer & B. D. Savage 1980; B. Wakker et al. 1998). Using 28 Hubble Space Telescope (HST)/Cosmic Origins Spectrograph (COS) sight lines of background quasars passing through the LMC, K22 found a declining column-density profile of high ions (including O VI, C IV, and Si IV) out to 35 kpc from the

* Based on archival observations made with the NASA/ESA Hubble Space Telescope, obtained from the Data Archive at the Space Telescope Science Institute, which is operated by the Association of Universities for Research in Astronomy, Inc., under NASA contract NAS5-26555. Archival funding was associated with program 17053.

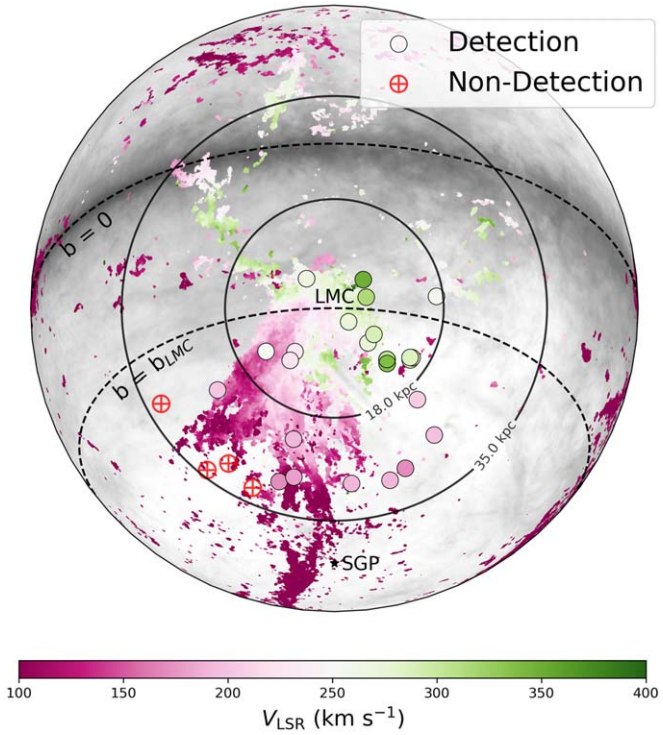

Figure 1. Velocity-coded map of the Magellanic System in an orthographic projection with LMC at the center, displaying the locations of 28 HST/COS background quasar sight lines (circles) from K22 with respect to the H I emission (color scale). The sight lines are color coded based on the column-density-weighted central LSR velocity of the Magellanic Si II absorption. Magellanic absorbers are those with $v_{\rm LSR} > 150$ km s^{-1} (see text in Section 2). Sight lines with Si II nondetections at Magellanic velocities are marked with red symbols with a cross. The map includes high-velocity 21 cm H I emission data from T. Westmeier (2018), color coded by LSR velocity.

LMC. They conclude that C IV and Si IV likely exist in the interfaces between the cooler ($\sim 10^4$ K) clouds and the hotter ($\sim 10^{5.5}$ K) corona traced directly by O VI. K22 found evidence for the cool LMC CGM but did not discuss this phase in detail. Its properties and connection to the warm/hot corona are crucial for developing a complete picture of the LMC CGM and the history of the LMC. In this Letter, we present the results from a detailed study of the cool LMC CGM and its connection to the Magellanic System.

2. Sample and Analysis

We use the published archival data set from K22 to map the CGM of the LMC. This data set includes HST/COS spectra of 28 UV-bright background quasars that probe the LMC up to 35 kpc distance from the LMC's center. This distance corresponds to an angular separation of approximately 45°. Sight lines beyond 45° are not included because at these large angles, geometrical distortions complicate the separation of absorption from the MW and the LMC. Figure 1 shows the location of these sight lines (circles) relative to the LMC at the center. All the sight lines except two (RX J0503.1–6634 and PKS 0552–640) probe the LMC CGM toward the Galactic south ($b < b_{\rm LMC}$). This is because high dust extinction from the MW hinders the identification of active galactic nuclei closer to the Galactic plane.

The data reduction steps for the COS spectra, including pipeline reduction, additional wavelength alignment, and removal of geocoronal airglow contamination in O I λ1302 and Si II λ1304, are based on the steps described in K22. To merge the G130M and G160M grating COS spectra for each quasar, we join the spectra at the wavelength where the average signal-to-noise ratio (SNR) per pixel from both gratings is approximately equal. Each quasar spectrum is binned by 3 pixels using the `Python` routine *SpectRes* (A. C. Carnall 2017). To fit a global continuum across individual quasar spectra, we employ a method similar to that outlined in S. Mishra & S. Muzahid (2022).

To trace the cool CGM of the LMC, we focus on the following transitions: O I λ1302; Fe II $\lambda\lambda$ 1143, 1144, 1608; Si II $\lambda\lambda$ 1190, 1193, 1260, 1304, 1526; Si III λ1206; Al II λ1670; S II $\lambda\lambda$ 1250, 1253; and Ni II $\lambda\lambda$ 1317, 1370. To identify the absorption associated with the Magellanic System, we impose a velocity threshold of $v_{\rm LSR} > 150$ km s^{-1} to avoid contamination from the MW and therefore separate the Galactic and Magellanic components (K. S. de Boer et al. 1990; B. P. Wakker & H. van Woerden 1997; N. Lehner & J. C. Howk 2011; P. Richter et al. 2015). For the maximum velocity threshold, we used $v_{\rm LSR} < 445$ km s^{-1}, which is calculated by finding the velocity dispersion around the LMC systematic velocity of 280 km s^{-1} that encloses 99.9% of Magellanic gas.

We use the Voigt-profile fitting software `VPFIT` (v12.3; R. F. Carswell & J. K. Webb 2014) to model these absorption profiles from the LMC CGM. Using a χ^2 minimization algorithm, `VPFIT` fits the line centroid, Doppler parameter (b), and column density (N) for each absorption component. To begin, we identify Magellanic components in each ion by visual inspection of the line profiles and then compare across ions of the same ionization state (low or high) to establish the component structure in each sight line. We then simultaneously fit multiple lines of the same ion. For lines from different ions, we tie the centroid velocity of the components only when they are aligned based on the visual inspection.

For all ions, we label components as saturated absorption if the normalized flux drops below 0.2 for at least three consecutive rebinned pixels. For ions with multiple transitions, we exclude the saturated components from the fitting process unless there are unsaturated components available from the weaker transitions. For ions with only one transition, we provide a lower limit for the column density if there is even a single saturated component (commonly the case for Si III). If there are velocity offsets between the transitions of the same ion falling on the G130M and G160M gratings, we applied a shift to align these transitions together. For nondetected transitions of an ion, we measure the 3σ upper limit using the SNR of the absorption-free region and assume the line extends over a width equal to the mean b value of detected transitions for that ion. The adopted upper limit for an ion with multiple transitions is taken from the upper limit from the strongest transition (with the highest oscillator strength) since this gives the strongest constraint.

The absorption parameters for the high ions C IV and Si IV are taken from K22. However, for the sight lines RBS 567 and IRAS Z06229–6434, we identify several additional Magellanic components, specifically two C IV components in each sight line and two and one Si IV components toward RBS 567 and IRAS Z06229–6434, respectively. We fit these new components in a similar manner to the low ions using `VPFIT`.

An example of our Voigt fits to the UV absorption-line profiles is shown in Figure 2 for the sight line toward 1H0419 −577, which passes 12.1 kpc from the LMC. These spectra show multiple Magellanic components in both the low and high

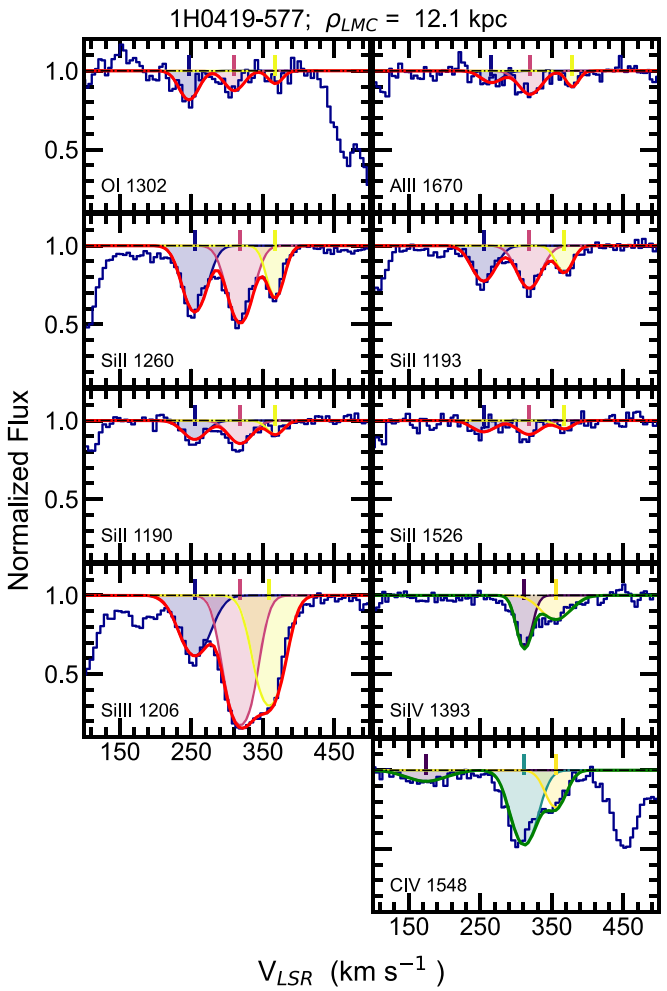

Figure 2. HST/COS metal-line profiles showing the absorption at Magellanic velocities toward 1H0419–577, as an example of our data quality and fitting methodology. Normalized flux is plotted against the LSR velocity in blue. The solid red lines represent the full Voigt-profile fits to the low ions from this study, while the solid green lines show the fits to the high ions from K22. The individual components are shaded in different colors, with centroids marked by tick marks. The color scheme differs between low and high ions.

ions. The relative strength of the low and high ions varies between components.

3. Results

We present in Figure 3 the total column density of the Magellanic components ($v_{\rm LSR} > 150\,{\rm km\,s^{-1}}$) for six low ions (O I, Al II, Fe II, Ni II, Si II, and S II) and one intermediate ion (Si III) plotted against both the impact parameter ($\rho_{\rm LMC}$, bottom x-axis) and the normalized impact parameter ($\rho_{\rm LMC}/R_{200}$,[12] top x-axis). We use $R_{200} = 115 \pm 15$ kpc for LMC (see K22). For comparison, we have included the column-density measurements for C IV and Si IV from K22 along with our new column-density estimates for these ions along the RBS 567 and IRAS Z06229–6434 sight lines. A declining column-density profile is observed in all nine ions shown.

To model our data set, we use Bayesian regression with censoring via the PyMC3 package (J. Salvatier et al. 2016). This approach effectively accounts for upper limits and lower limits in our data. PyMC3 is a Python-based probabilistic programming framework, which employs Markov Chain Monte Carlo (MCMC) and variational inference algorithms to estimate the posterior distributions of model parameters. A detailed illustration of this method is described in Y. Zheng et al. (2024a; see their Appendix C). For each ion profile, we model the column density (log N) and impact parameter ($\rho_{\rm LMC}$) simultaneously for detections, lower limits from saturated absorption, and upper limits from nondetections using a log–linear relation (exponential fit), mathematically expressed as $\log\,(N/{\rm cm^{-2}}) = c + m\,(\rho_{\rm LMC}/{\rm kpc})$. A declining trend in the total column density with increasing $\rho_{\rm LMC}$ for all the ions is evident in Figure 3. The slopes of the log–linear relation for the low and intermediate ions are consistent with each other within 1σ. Additionally, the column-density profiles for low and intermediate ions are steeper compared to those for high ions, as indicated by the slopes of the fits, with the only exception being the Ni II profiles. However, since Ni II is detected along only four quasar sight lines, the fit has higher uncertainty, and hence, we do not infer anything conclusive from the Ni II profile.

Next, we explore the LMC CGM kinematics using the measured velocity centroids of low and high ions. In Figure 4, we show the centroid velocities of individual components with $v_{\rm LSR} > 150\,{\rm km\,s^{-1}}$ as a function of $\rho_{\rm LMC}$ for Si II, Si III, Si IV, and C IV. These four ions are chosen to represent gas in different phases although the results are consistent with all nine ions presented in Figure 3. We observe more kinematic complexity, indicated by more velocity components, closer to the LMC (with an average of ∼three components per sight line for $\rho_{\rm LMC} < 17$ kpc) compared to farther regions (with an average of ∼one component per sight line for $\rho_{\rm LMC} > 17$ kpc). This result holds separately for low, intermediate, and high ions. The dispersions in the velocity centroids for <17 kpc (>17 kpc) are $67\,{\rm km\,s^{-1}}$ ($42\,{\rm km\,s^{-1}}$) for low, $65\,{\rm km\,s^{-1}}$ ($43\,{\rm km\,s^{-1}}$) for intermediate, and $67\,{\rm km\,s^{-1}}$ ($42\,{\rm km\,s^{-1}}$) for high ions, respectively. The mean and standard deviation of centroid velocities of individual LMC CGM components in Si II, Si III, Si IV, and C IV are 276 ± 71, 281 ± 71, 275 ± 60, and $281 \pm 72\,{\rm km\,s^{-1}}$, respectively, all closely consistent with each other.

We then estimate the column-density-weighted velocity centroids, defined as $v_{\rm weighted} = \frac{\Sigma(v_{\rm comp} \times N_{\rm comp})}{\Sigma\ N_{\rm comp}}$, for each sight line, to give an estimate of the *mass-weighted average velocity* of the Magellanic gas. In Figure 4, we plot these weighted velocities for the ions as a function of $\rho_{\rm LMC}$. The mean and standard deviation of the weighted velocity for the four ions are consistent with each other, with an average value of $274 \pm 56\,{\rm km\,s^{-1}}$. In Figure 4, the horizontal black dashed–dotted line indicates the systematic velocity of the LMC of $280\,{\rm km\,s^{-1}}$, with the shaded gray region representing the $\pm 50\,{\rm km\,s^{-1}}$ region around it, consistent with our average dispersion of $56\,{\rm km\,s^{-1}}$ for the LMC in all phases. From the figure, we observe a drop near 17 kpc (shown as a shaded region in magenta) where the N-weighted centroids fall sharply for all ions, with the gas farther out only observed at lower LSR velocities. We confirm that the velocity distributions of absorbers inside and outside 17 kpc differ significantly at the 99.9% confidence level using a two-sample Kolmogorov–Smirnov test. We argue in Section 4 that the gas beyond 17 kpc mostly traces the stripped gas in the Stream. Therefore, in Section 4, we use a more restrictive limit of $v > 230\,{\rm km\,s^{-1}}$ to identify the gas with the (nonstripped) LMC CGM.

[12] R_{200} is the radius enclosing a mean overdensity of 200 times the critical density.

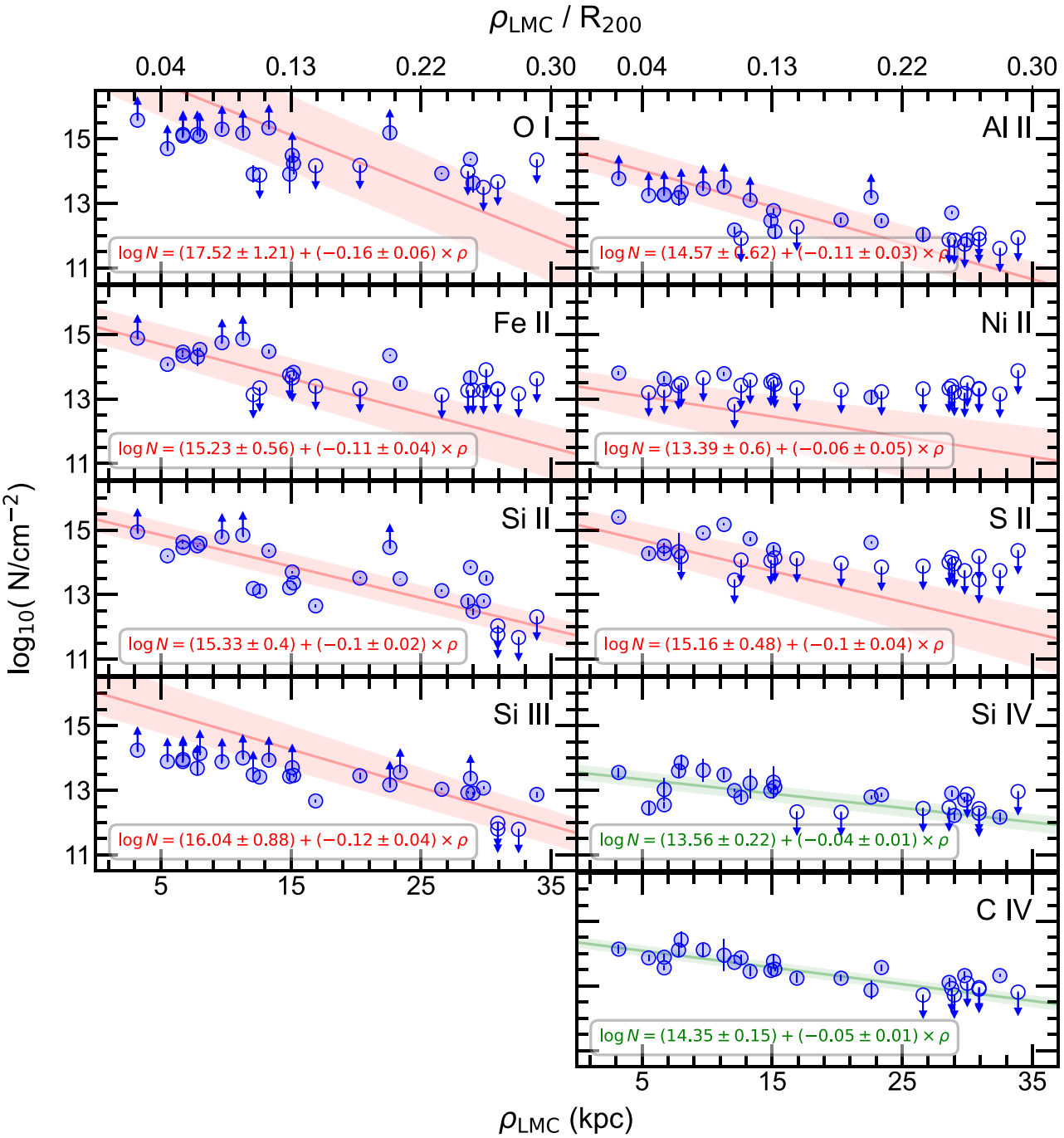

Figure 3. Total column density of Magellanic gas as a function of LMC impact parameter. The profiles of six low ions and one intermediate ion (Si III) are shown in red. For comparison, the profiles for the high ions Si IV and C IV are included in green; these data are taken from K22 along with additional C IV and Si IV components identified toward RBS 567 and IRAS Z06229–6434. Open circles with downward arrows indicate 3σ upper limits, while circles with upward arrows represent lower limits from saturated lines. The best-fit log–linear relations for MCMC runs with 1σ scatter (shaded regions) are shown as solid lines with the relation labeled in the bottom left corner of each panel. The best-fit relations using the normalized impact parameter instead of $\rho_{\rm LMC}$ are the same with the slopes scaled by $R_{200} = 115 \pm 15$ kpc (see K22). In this plot, Magellanic components are defined as those with $v_{\rm LSR} > 150$ km s^{-1}.

4. Discussion

The relationship between metal-line column density and impact parameter has been widely used to characterize the CGM of galaxies (e.g., J. X. Prochaska et al. 2011; J. Tumlinson et al. 2013). Figure 3 shows this relationship for six low, one intermediate, and two high ions in the LMC CGM. We find a declining trend in these profiles as inferred from the slope of the log–linear fits given in each panel. The declining column-density profile is a characteristic signature of the CGM (J. Tumlinson et al. 2017). We note that all our sight lines probe at least 3° (i.e., $\gtrsim$3 kpc) off the LMC, which is beyond the known extent of LMC winds arising from stellar feedback (see K. A. Barger et al. 2016; Y. Zheng et al. 2024b).

From the slopes of the LMC column-density profiles (Figure 3), the following observations can be made: (1) All the low-ion and intermediate-ion profiles have similar slopes, consistent within the errors. (2) The high-ion slopes from Si IV

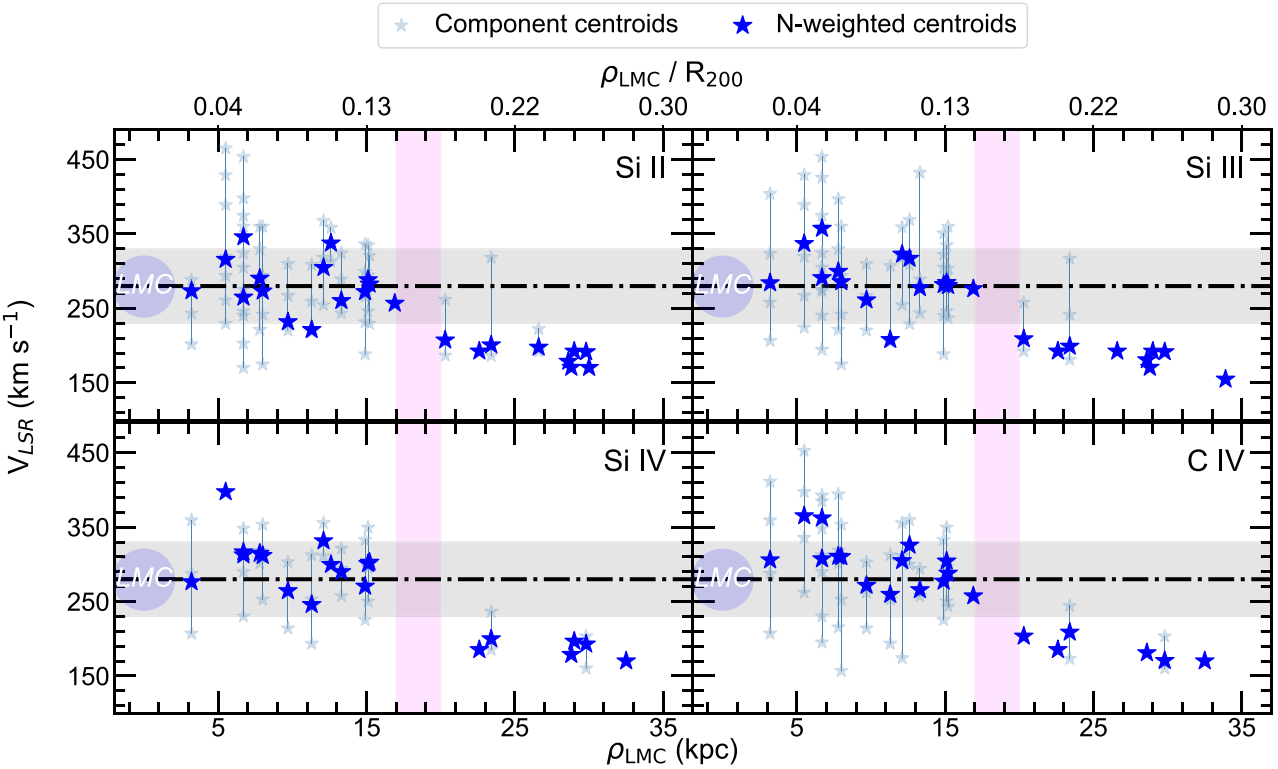

Figure 4. Velocity-position analysis of gas in the LMC CGM. LSR velocity is plotted against LMC impact parameter both for individual components (steel-blue stars) and for the column-density-weighted central velocity of all Magellanic components along each sight line (large blue stars). The solid vertical lines in steel blue connect the different velocity components of each sight line and illustrate the dispersion of LMC gas in each direction. The horizontal dashed–dotted black line represents the LMC systemic velocity of 280 km s^{-1}. The shaded gray area indicates the region within ±50 km s^{-1} of the LMC velocity. The shaded area in magenta marks the region where the gas velocities change substantially; this truncation point separates the inner CGM from the Stream.

and C IV are consistent with each other. (3) The low-ion slopes are steeper by a factor of 2 than the high-ion slopes (similar to the M31 CGM; N. Lehner et al. 2020). The declining column-density profiles with ρ_{LMC} are seen for *all* ions at 3σ significance (see Figure 3).

One interpretation of the declining column-density profiles across multiple ions is that the gas originates from the multiphase CGM of the LMC. The steeper slope of the low ions compared to the high ions indicates that the LMC CGM is (relatively) more ionized at larger distances. One possible multiphase CGM model is the interface or boundary-layer scenario as favored by K22, where high ions, such as Si IV and C IV, arise at the turbulent or conductive interfaces between 10^4 K low-ion clouds and the hot $\approx 10^{5.5}$ K diffuse gas of the Magellanic Corona (e.g., K. Kwak et al. 2015; C.-A. Faucher-Giguère & S. P. Oh 2023). This interface scenario is consistent with our kinematic findings shown in Figure 4, which show that the low and high ions are kinematically related. On the other hand, the flatter profiles of high ions compared to low ions may also result if the high-ion gas includes components produced by both photoionization and collisional ionization. However, K22 found that the influence of photoionization is strongest within 7 kpc of the LMC, while beyond that distance, the gas traced by Si IV and C IV is almost entirely collisionally ionized, making this explanation less likely.

In our kinematic analysis (Figure 4), the weighted centroid velocities drop sharply beyond 17 kpc for both low ions and high ions, with absorbers beyond 17 kpc predominantly found at LSR velocities <230 km s^{-1}. We confirm that this decrease is neither due to the reduced number of sight lines beyond 17 kpc (see Figure 1) nor to a decrease in the sensitivity of the spectra beyond 17 kpc. These lower-velocity absorbers are associated with the Magellanic Stream, as seen in Figure 1. Sight lines within 17 kpc of the LMC show Si II at the LMC's systemic velocity of 280 km s^{-1}. Beyond 17 kpc, the Si II absorbers have much lower velocities, consistent with the Stream. To explore the role of the Stream in more detail, we examined the low- and high-ion column densities as a function of impact parameter for absorbers with velocities between 150 and 230 km s^{-1} (i.e., Stream velocities). These profiles do not show a significant declining trend with ρ_{LMC}. In addition, we find no correlation between the column density and ρ_{LMC} for these lower-velocity absorbers using the Spearman rank correlation test, further indicating that the gas beyond 17 kpc is associated with the Stream rather than the LMC.

In principle, the compactness of a galaxy's CGM can be explained by: (i) the galaxy not being massive enough to retain a larger CGM that extends up to its virial radius (see R. Bordoloi et al. 2014), and/or (ii) the CGM being truncated due to strong interactions with the surrounding environment. Since it is now well established that the LMC is an intermediate-mass galaxy with $M_{halo} > 10^{11}\,M_{\odot}$ (D. Erkal et al. 2019; L. L. Watkins et al. 2024), the first scenario is unlikely, leaving environmental effects as the likely explanation for the compactness of the LMC CGM.

To explore the environmental effects, we compare the CGM of the LMC with that of isolated dwarf galaxies using the recent sample of Y. Zheng et al. (2024a), which focuses on the metal content in the CGM of nearby dwarf galaxies. This

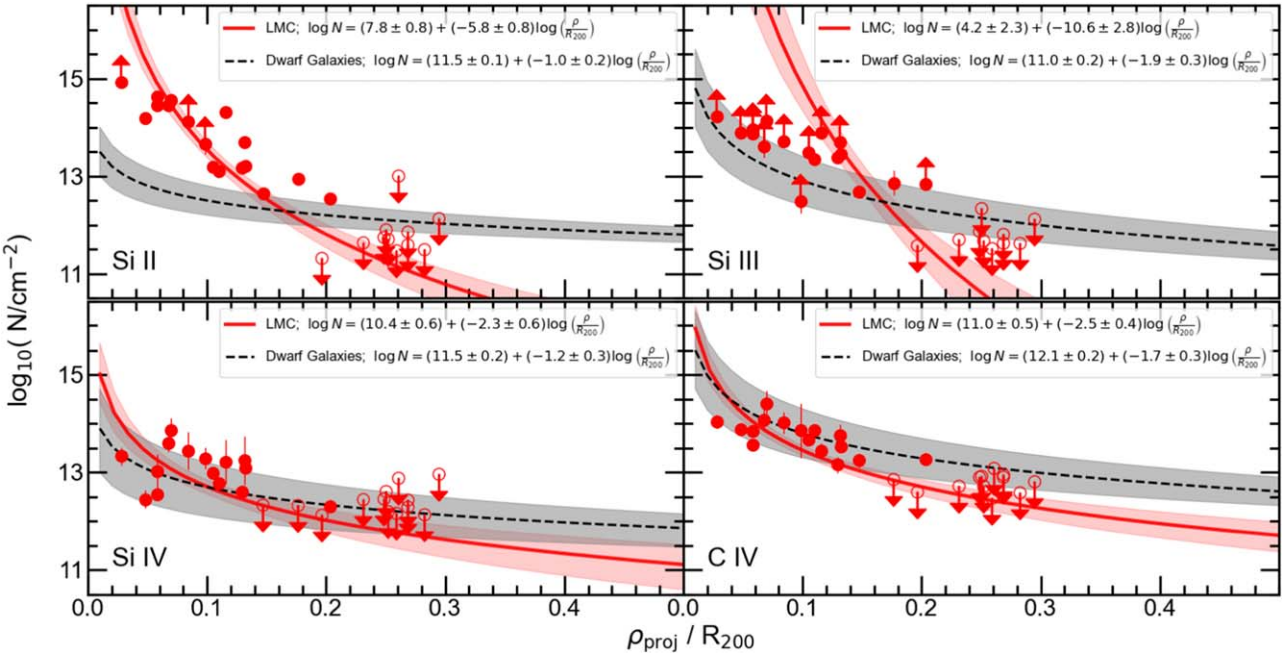

Figure 5. Column-density profiles of the CGM in four low ions, comparing the LMC to isolated dwarf galaxies in the literature. The red points show the total column density of LMC components at $v_{\rm LSR} > 230$ km s^{-1} (a range chosen to exclude the Stream) as a function of impact parameter normalized by the virial radius. Open symbols indicate the 3σ upper limits for nondetections. The 50th percentile solution of the power-law model for MCMC runs for the LMC is shown in the red solid line with 1σ scatter of the fit shown in shaded red. For comparison, the profiles from the CGM of isolated dwarf galaxies taken from Y. Zheng et al. (2024a) are shown in black in each panel with 1σ uncertainty in gray.

sample consists of 45 isolated dwarf galaxies with 56 galaxy–quasar pairs having $z = 0.0$–0.3 and mass range of $M_* \approx 10^{6.5-9.5}\,M_\odot$, including the COS-Dwarfs sample (R. Bordoloi et al. 2014). For the LMC CGM, we do not impose any impact parameter cut to ensure an unbiased comparison with the isolated dwarf galaxy sample, but we only include absorbers with $v_{\rm LSR} > 230$ km s^{-1} to exclude Stream contributions. For sight lines beyond 17 kpc, we treat them as nondetections and estimate upper limits at the LMC's systematic velocity of 280 km s^{-1}. In Figure 5, we show the total column density of Si II, Si III, Si IV, and C IV as a function of normalized impact parameter. To compare the corresponding column-density profiles for the isolated dwarf galaxies, we used the best-fit log–log relation (power-law fit) presented in Figure 4 of Y. Zheng et al. (2024a), which has the form $\log N = \log N_0 + k \log \frac{\rho}{R_{200}}$. We see clearly that the LMC profiles are steeper than the profiles of the isolated dwarf galaxies. This difference is strongest for the low-ion Si II, also strong for the intermediate-ion Si III, and still present but weaker for the high-ion Si IV. The distinct differences in the profile of the LMC halo compared to other dwarf galaxies can be attributed to the strong dynamical interactions of the LMC with the MW and SMC, i.e., to the highly nonisolated nature of the LMC. Therefore, our observations of a steep column-density profile for the LMC CGM, despite its higher stellar mass and halo mass than the galaxies in the Y. Zheng et al. (2024a) sample, suggest that strong environmental effects are disturbing and stripping the LMC CGM.

The 17 kpc truncation radius of the LMC CGM can be understood as a ram-pressure effect. A recent simulation by J. Zhu et al. (2024) estimates the survival of an LMC-like CGM against ram-pressure stripping in an MW-type environment (see their Section 5.4). By employing an isothermal spherical CGM with a power-law density profile (power-law index of −2) and using a pericentric ram-pressure value of $P_{\rm ram} \approx 2 \times 10^{-13}$ dyne cm^{-2} (M. Salem et al. 2015), the authors predict a maximum CGM stripping radius of 15 kpc, which aligns well with our observed LMC truncation radius of 17 kpc. The authors found only 10% of the initial CGM mass survives. It is noteworthy that the LMC's CGM may no longer be spherical and could be compressed toward the front (i.e., north side with $b > b_{\rm LMC}$), as is evident from the generation of bow shocks (D. J. Setton et al. 2023). Nonetheless, our observed LMC CGM truncation radius of 17 kpc is also in reasonable agreement with the simulations of S. Lucchini et al. (2020, 2024) and C. Carr et al. (2024), which account for this front-side compression. Specifically, the LMC corona in S. Lucchini et al. (2024) extends ≈20° to either side of the LMC, corresponding to ∼18 kpc at the LMC distance. However, this region toward the north ($b > b_{\rm LMC}$) currently lacks UV sight lines (see Figure 1) and therefore remains unprobed observationally. We have an approved HST/COS Cycle 32 program to probe the LMC CGM in this region (PI: S. Mishra).

5. Summary

We have presented new findings on the LMC CGM using HST/COS G130M and G160M spectra of 28 quasar sight lines extending up to 35 kpc from the LMC. We trace the cool ($\sim 10^4$ K) gas using six low ions: O I, Al II, Fe II, Ni II, Si II, and S II and one intermediate ion: Si III. Our results are supplemented by high-ion data (Si IV and C IV) from K22. We observe a declining column-density profile for both low-ion and high-ion column densities as a function of the impact parameter, with the low ions declining more steeply than the high ions. The kinematic structure of both the cool and warm

phases becomes more complex closer to the LMC compared to larger impact parameters.

Importantly, we observe a break in the LMC CGM properties at 17 kpc. Inside 17 kpc, the CGM absorption is found within $\approx$50 km s^{-1} of the LMC systemic velocity of 280 km s^{-1}. Beyond 17 kpc, the absorption is predominantly found at the much lower velocities ($<$230 km s^{-1}) of the Stream, indicating a clear truncation in the LMC CGM at this distance. The truncation radius is in good agreement with recent simulations (S. Lucchini et al. 2020, 2024; C. Carr et al. 2024; J. Zhu et al. 2024). Our finding of a truncated LMC CGM supports the picture of a high-mass LMC on its first infall passage that has lost most (but not all) of its CGM to ram-pressure stripping by the MW halo. As a result, the MW halo has gained mass, but the LMC halo has still survived. The survival of a small halo is important for the LMC's evolution, as the halo protects its interstellar gas from being stripped and allows star formation in the LMC to continue.

Acknowledgments

We thank the referees for their constructive and helpful reports. Support for program 17053 was provided by NASA through a grant from the Space Telescope Science Institute, which is operated by the Association of Universities for Research in Astronomy, Inc., under NASA contract NAS5-26555.

Appendix

The stack plots for the remaining sight lines are shown in Figures A1–A6. In Table A1, we present the Voigt-fit parameters for all Magellanic absorption components ($v_{\rm LSR} > 150$ km s^{-1}) in the sample.

Table A1
Absorption Parameters of Magellanic Components Derived from Voigt-profile Fitting

Quasar Name	GLON (deg)	GLAT (deg)	ρ (kpc)	Ion	$v_{\rm LSR}$ (km s^{-1})	b (km s^{-1})	log N (cm^{-2})	References
(1)	(2)	(3)	(4)	(5)	(6)	(7)	(8)	(9)
RX J0503.1−6634	277.18	−35.42	3.2	O I	229.6 ± 15.1	46.8 ± 1.6	>15.18	This work
				O I	296.6 ± 13.8	51.0 ± 2.5	>15.34	This work
				O I	374.4 ± 2.3	10.1 ± 3.6	13.54 ± 0.19	This work
				Al II	162.6 ± 3.2	36.7 ± 56.2	12.34 ± 0.57	This work
				Al II	204.7 ± 2.8	10.7 ± 4.7	12.31 ± 0.27	This work
…	…	…	…	…	…	…	…	…

Note. Column (1): quasar name. Columns (2)–(3): galactic longitude and latitude. Column (4): impact parameter. Column (5): name of the ion. Columns (6)–(8): centroid velocity, line width, and column density of absorption component from VPFIT. Column (9): references for the measurements.

(This table is available in its entirety in machine-readable form in the online article.)

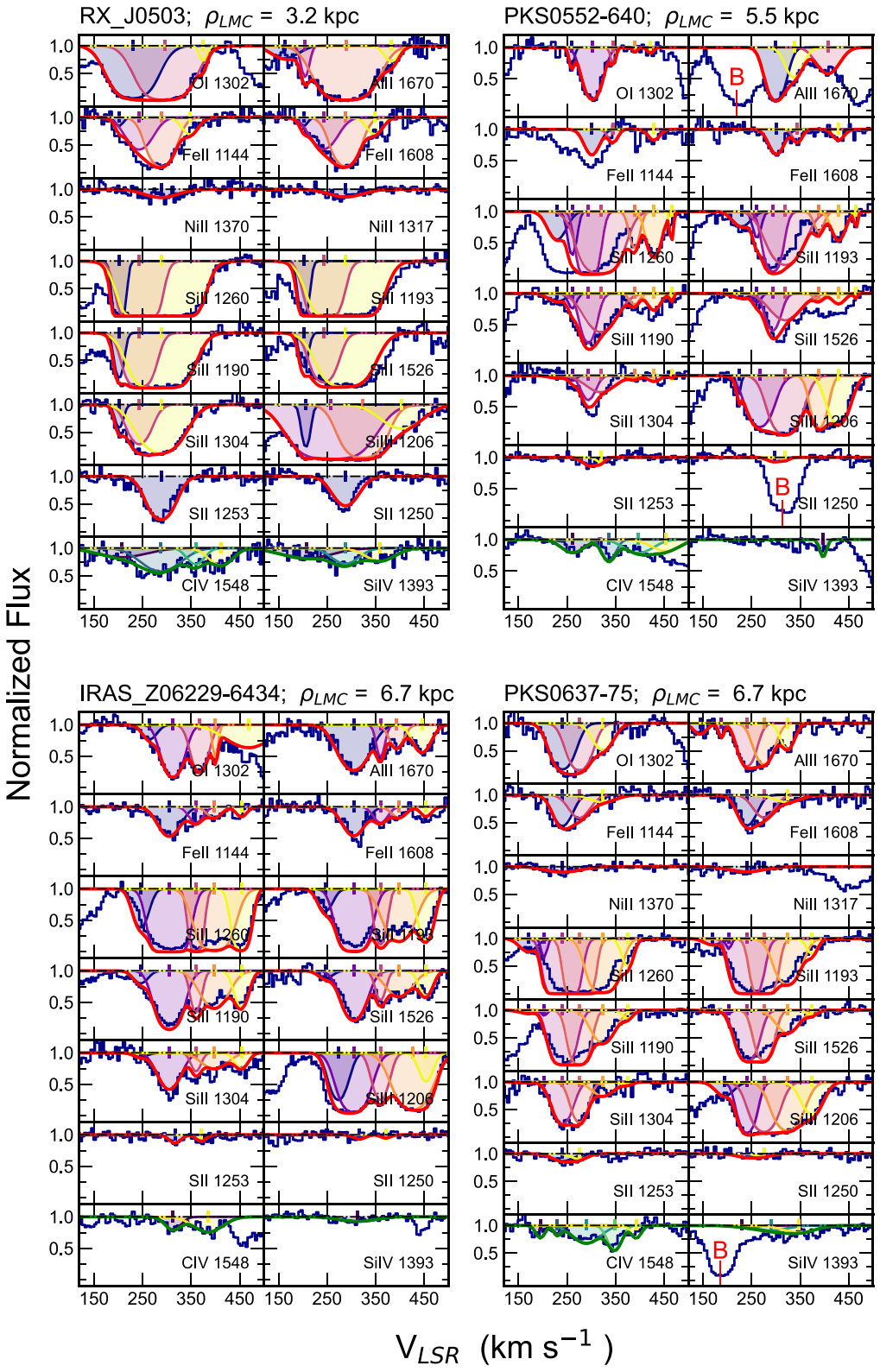

Figure A1. Same as Figure 2. We indicate the locations of blended regions with "B" in red and exclude these regions from the fitting.

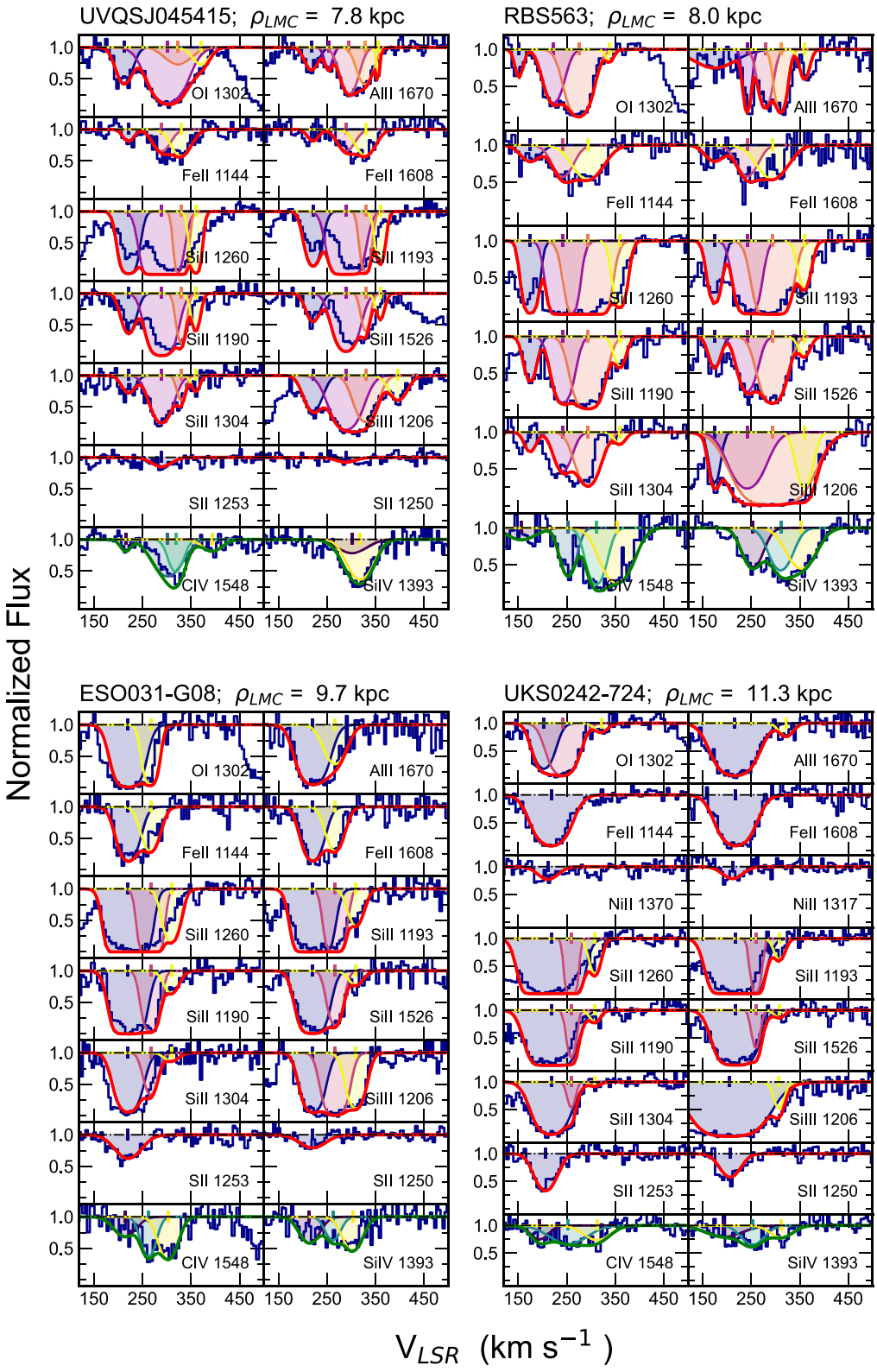

Figure A2. Same as Figure 2.

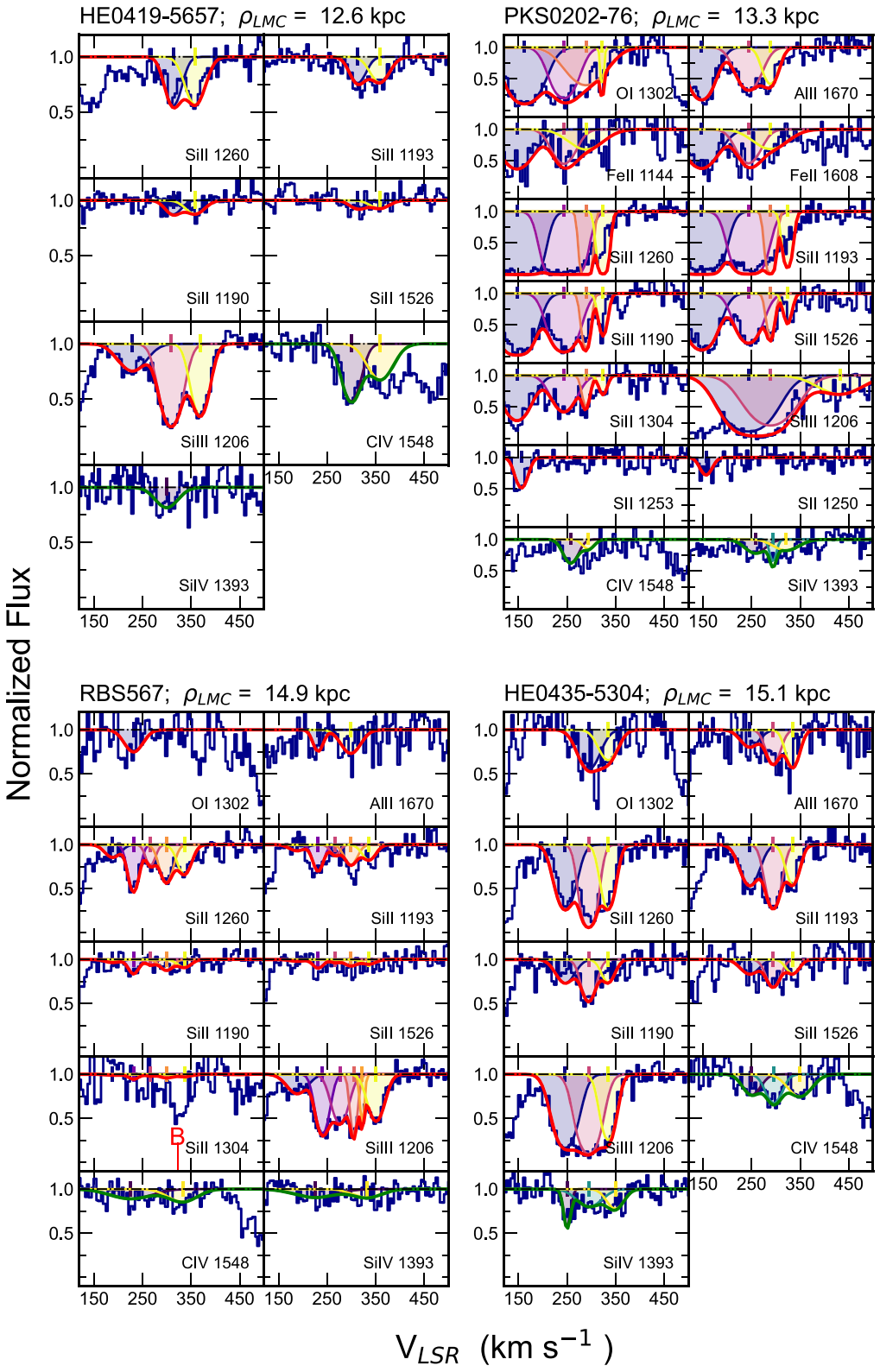

Figure A3. Same as Figure 2.

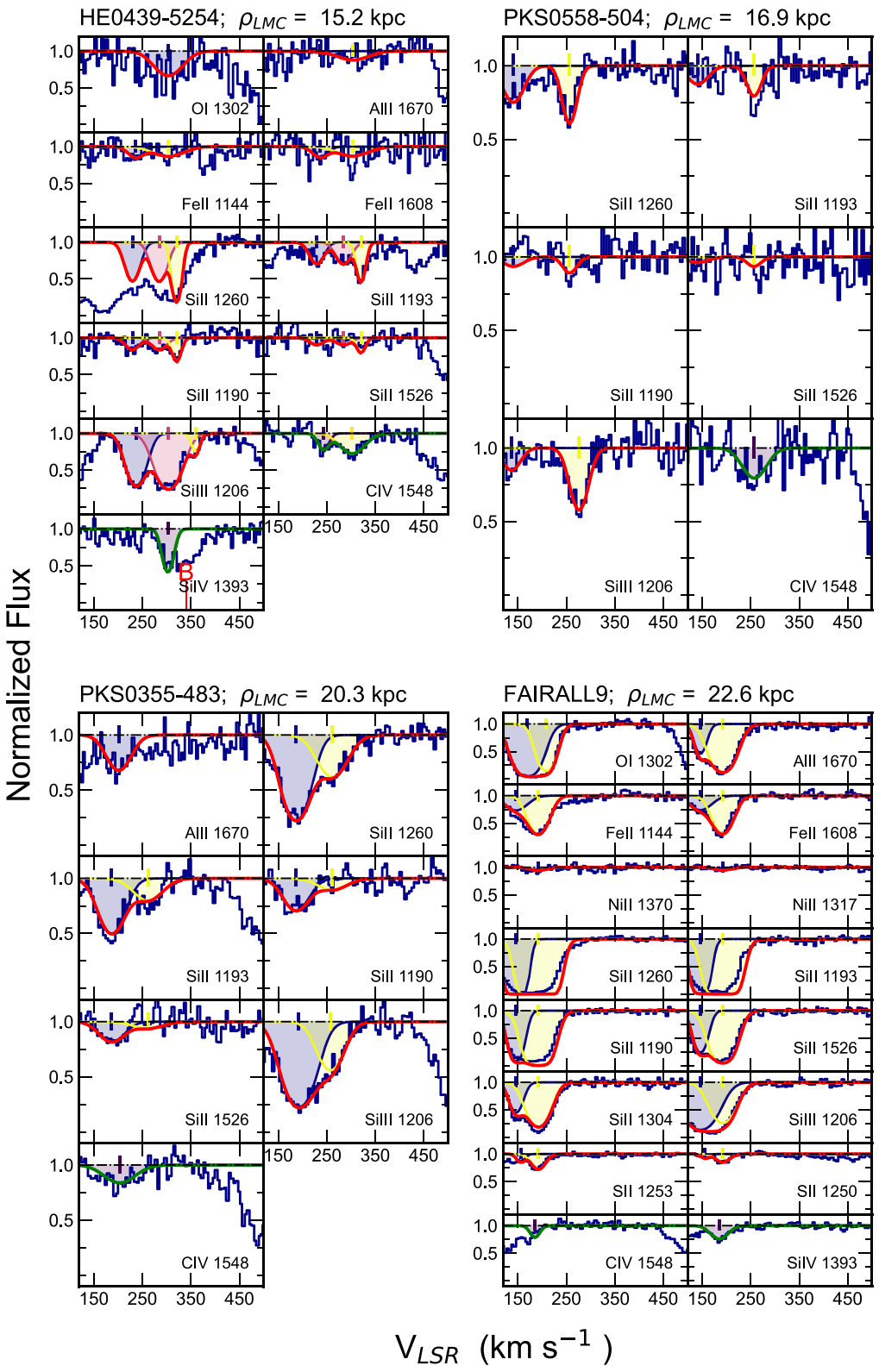

Figure A4. Same as Figure 2.

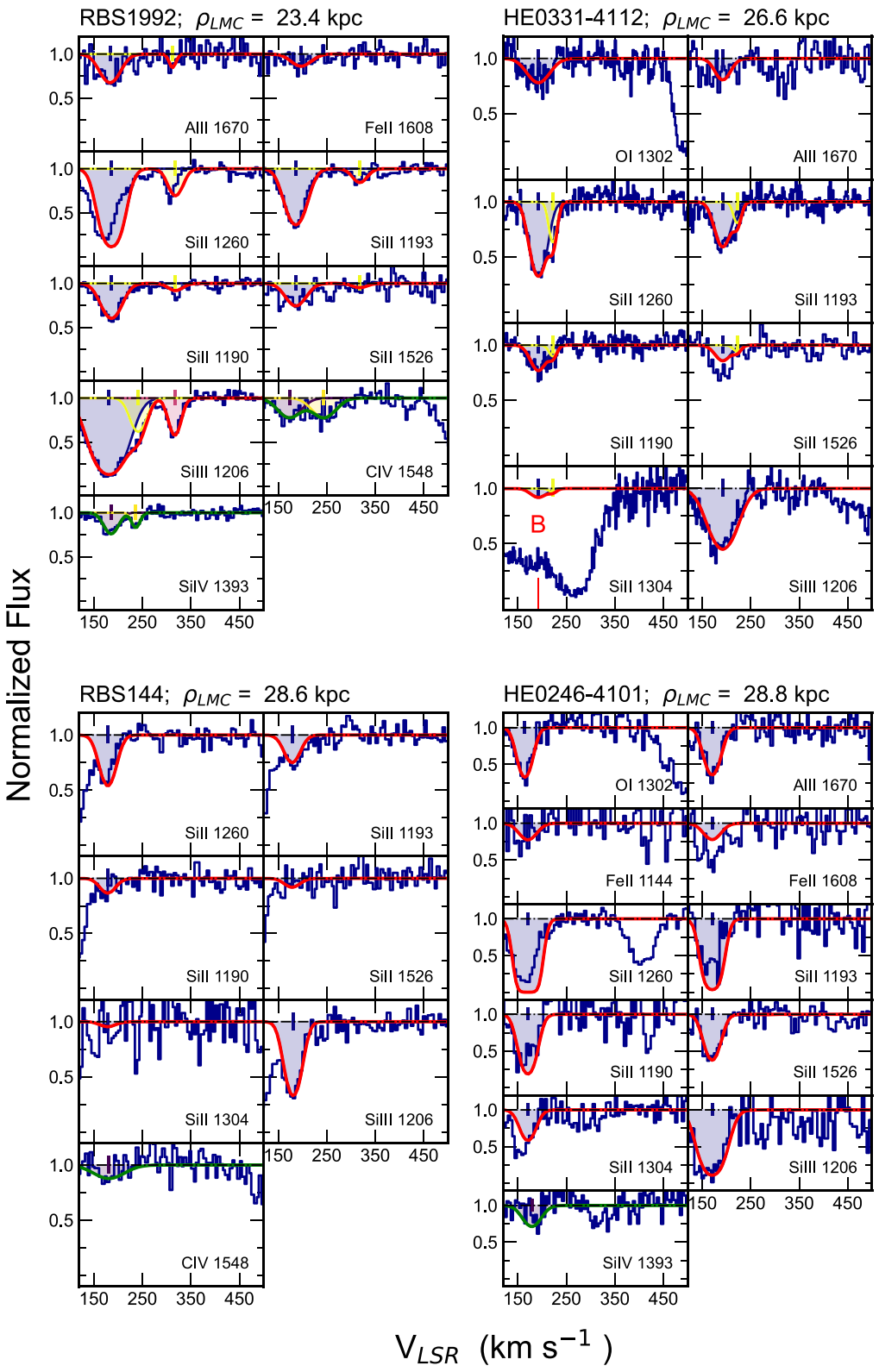

Figure A5. Same as Figure 2.

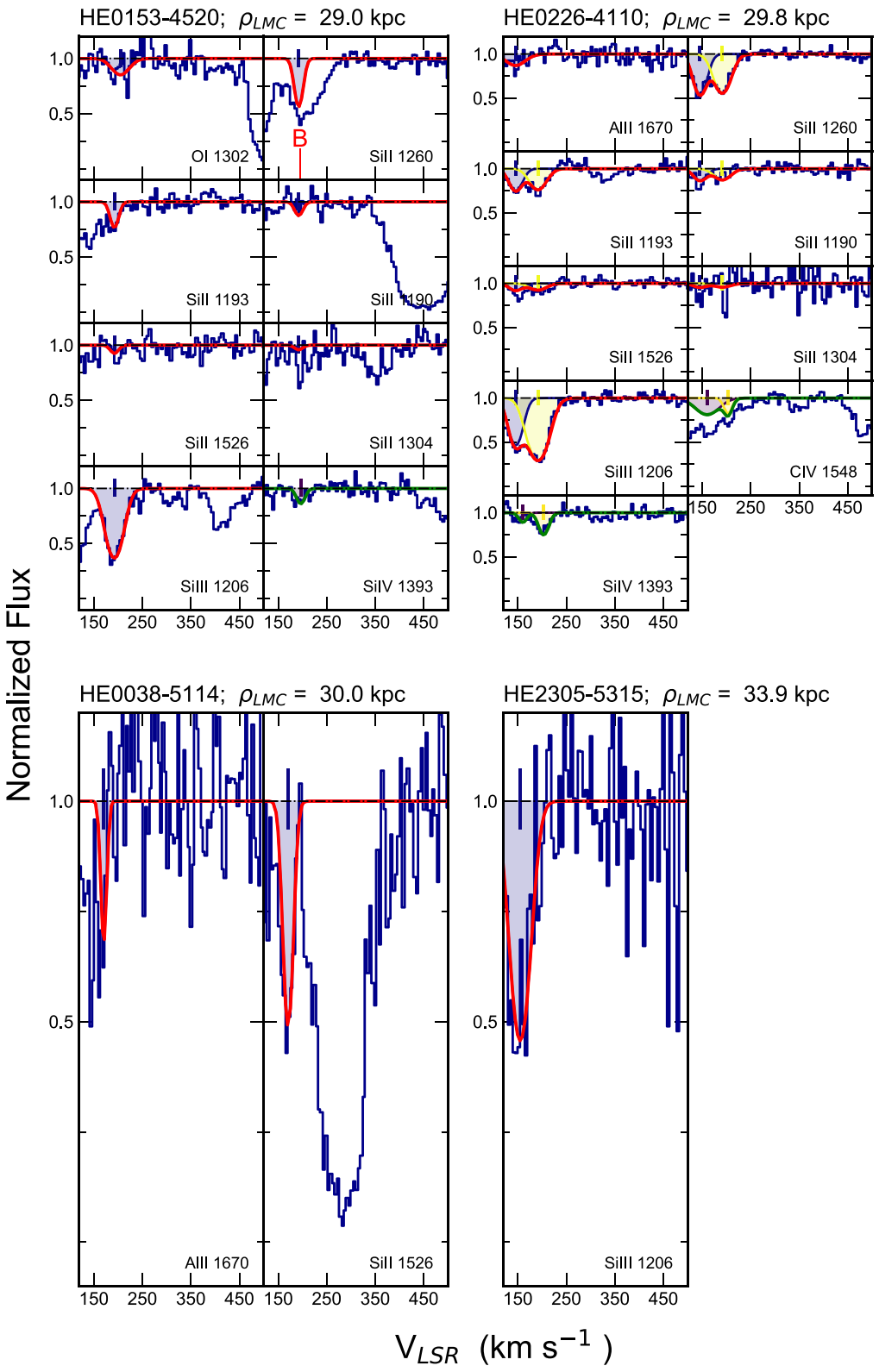

Figure A6. Same as Figure 2.

ORCID iDs

Sapna Mishra https://orcid.org/0000-0002-4157-5164
Andrew J. Fox https://orcid.org/0000-0003-0724-4115
Dhanesh Krishnarao https://orcid.org/0000-0002-7955-7359
Scott Lucchini https://orcid.org/0000-0001-9982-0241
Elena D'Onghia https://orcid.org/0000-0003-2676-8344
Frances H. Cashman https://orcid.org/0000-0003-4237-3553
Kathleen A. Barger https://orcid.org/0000-0001-5817-0932
Nicolas Lehner https://orcid.org/0000-0001-9158-0829
Jason Tumlinson https://orcid.org/0000-0002-7982-412X

References

Barger, K. A., Lehner, N., & Howk, J. C. 2016, ApJ, 817, 91
Barger, K. A., Madsen, G. J., Fox, A. J., et al. 2017, ApJ, 851, 110
Besla, G., Kallivayalil, N., Hernquist, L., et al. 2012, MNRAS, 421, 2109
Bland-Hawthorn, J., Maloney, P. R., Sutherland, R., et al. 2019, ApJ, 886, 45
Bordoloi, R., Tumlinson, J., Werk, J. K., et al. 2014, ApJ, 796, 136
Brüns, C., Kerp, J., Staveley-Smith, L., et al. 2005, A&A, 432, 45
Carnall, A. C. 2017, arXiv:1705.05165
Carr, C., Bryan, G. L., Garavito-Camargo, N., et al. 2024, arXiv:2408.10358
Carswell, R. F., & Webb, J. K. 2014, VPFIT: Voigt Profile Fitting Program, Astrophysics Source Code Library, ascl:1408.015
de Boer, K. S., Morras, R., & Bajaja, E. 1990, A&A, 233, 523
de Boer, K. S., & Savage, B. D. 1980, ApJ, 238, 86
Diaz, J., & Bekki, K. 2011, PASA, 28, 117
D'Onghia, E., & Fox, A. J. 2016, ARA&A, 54, 363
Erkal, D., Belokurov, V., Laporte, C. F. P., et al. 2019, MNRAS, 487, 2685
Faucher-Giguère, C.-A., & Oh, S. P. 2023, ARA&A, 61, 131
Fox, A. J., Richter, P., Wakker, B. P., et al. 2013, ApJ, 772, 110
Fox, A. J., Wakker, B. P., Barger, K. A., et al. 2014, ApJ, 787, 147
Fujimoto, M., & Sofue, Y. 1977, A&A, 61, 199
Kim, D. A., Zheng, Y., & Putman, M. E. 2024, ApJ, 966, 134
Krishnarao, D., Fox, A. J., D'Onghia, E., et al. 2022, Natur, 609, 915
Kwak, K., Shelton, R. L., & Henley, D. B. 2015, ApJ, 812, 111
Lehner, N., Berek, S. C., Howk, J. C., et al. 2020, ApJ, 900, 9
Lehner, N., & Howk, J. C. 2011, Sci, 334, 955
Lucchini, S., D'Onghia, E., & Fox, A. J. 2024, ApJ, 967, 16
Lucchini, S., D'Onghia, E., Fox, A. J., et al. 2020, Natur, 585, 203
Mishra, S., & Muzahid, S. 2022, ApJ, 933, 229
Moore, B., & Davis, M. 1994, MNRAS, 270, 209
Nidever, D. L., Majewski, S. R., & Butler Burton, W. 2008, ApJ, 679, 432
Nidever, D. L., Majewski, S. R., Butler Burton, W., & Nigra, L. 2010, ApJ, 723, 1618
Pardy, S. A., D'Onghia, E., & Fox, A. J. 2018, ApJ, 857, 101
Petersen, M. S., & Penarrubia, J. 2021, NatAs, 5, 251
Pietrzyński, G., Graczyk, D., Gieren, W., et al. 2013, Natur, 495, 76
Prochaska, J. X., Weiner, B., Chen, H. W., Mulchaey, J., & Cooksey, K. 2011, ApJ, 740, 91
Putman, M. E., Bland-Hawthorn, J., Veilleux, S., et al. 2003a, ApJ, 597, 948
Putman, M. E., Staveley-Smith, L., Freeman, K. C., Gibson, B. K., & Barnes, D. G. 2003b, ApJ, 586, 170
Richter, P., de Boer, K. S., Werner, K., & Rauch, T. 2015, A&A, 584, L6
Richter, P., Fox, A. J., Wakker, B. P., et al. 2013, ApJ, 772, 111
Salem, M., Besla, G., Bryan, G., et al. 2015, ApJ, 815, 77
Salvatier, J., Wieckiâ, T. V., & Fonnesbeck, C. 2016, PyMC3: Python Probabilistic Programming Framework, Astrophysics Source Code Library, ascl:1610.016
Setton, D. J., Besla, G., Patel, E., et al. 2023, ApJL, 959, L11
Tumlinson, J., Peeples, M. S., & Werk, J. K. 2017, ARA&A, 55, 389
Tumlinson, J., Thom, C., Werk, J. K., et al. 2013, ApJ, 777, 59
Wakker, B., Howk, J. C., Chu, Y.-H., Bomans, D., & Points, S. D. 1998, ApJL, 499, L87
Wakker, B. P., & van Woerden, H. 1997, ARA&A, 35, 217
Wang, J., Hammer, F., Yang, Y., et al. 2019, MNRAS, 486, 5907
Watkins, L. L., van der Marel, R. P., & Bennet, P. 2024, ApJ, 963, 84
Westmeier, T. 2018, MNRAS, 474, 289
Zheng, Y., Faerman, Y., Oppenheimer, B. D., et al. 2024a, ApJ, 960, 55
Zheng, Y., Tchernyshyov, K., Olsen, K., et al. 2024b, ApJ, 974, 22
Zhu, J., Tonnesen, S., Bryan, G. L., & Putman, M. E. 2024, ApJ, 974, 142